Electronic Supplementary Material (ESI) for Chemical Communications.
This journal is © The Royal Society of Chemistry 2023

Supplementary Information

Iron-optimized Oxygen Vacancy Concentration to Strength the Electrocatalytic Ability of Urea Oxidation Reaction

Yingzhen Zhang [1a], Wei Zhang [1a], Yonggang Lei [a], Jianying Huang [a,b*], Zhiqun Lin [c*], and Yuekun Lai [a,b*]

[a] National Engineering Research Center of Chemical Fertilizer Catalyst (NERC-CFC), College of Chemical Engineering, Fuzhou University, Fuzhou 350116, P.R. China

[b] Qingyuan Innovation Laboratory, Quanzhou 362801, P.R. China

[c] Department of Chemical and Biomolecular Engineering, National University of Singapore, Singapore 117585, Singapore

[1] These authors contributed equally to this work.

[*]Corresponding authors: yklai@fzu.edu.cn; jyhuang@fzu.edu.cn; z.lin@nus.edu.sg

1. Experimental

1.1. Materials

The chemicals utilized in the experiment were as follows: nickel(II) sulfate hexahydrate ($NiSO_4 \cdot 6H_2O$, AR, Aladdin), iron(III) nitrate nonahydrate ($Fe(NO_3)_3 \cdot 9H_2O$, 98.0%, Adamas-beta), selenium powder (Se, 99.99%, Aladdin), urea (CH_4N_2O, AR, Sinopharm), N,N-Dimethylformamide (DMF, AR, Sinopharm) and hydrazine hydrate ($N_2H_4 \cdot H_2O$, 85.0%, Sinopharm). These chemicals were used without undergoing any further purification processes. Nickel foam (NF) with a thickness of 2 mm served as the self-standing electrode substrate for the electrodeposition process.

1.2 Preparation of Catalysts

1.2.1. Synthesis of $NiSe_2$ Nanorods

In-situ crafting of $NiSe_2$ nanorods on NF surface by hydrothermal method involves the following steps. Firstly, the NF (4*6 cm^2) was cleaned to remove any contaminants by 3.0 M HCl, absolute ethanol and H_2O, respectively. This cleaning process ensures a clean surface of NF for the subsequent deposition of $NiSe_2$ nanorods. Secondly, the reaction mixture containing 100 mL of N,N-dimethylformamide (DMF), 0.84 mL of hydrazine, and 3.75 mmol of selenium powder was prepared. Thirdly, the resulting solution was then transferred into a 200 mL Teflon-polytetrafluoroethylene reactor, heated to 180 °C and react for 1 h. After the reaction, naturally cool to ambient temperature. Then, the $NiSe_2$ nanorods were washed several times by ultrapure water and absolute ethanol to remove any residual reactants, and dried under vacuum at 60 °C.

1.2.2. Synthesis of Iron-Modified $Ni(OH)_2$@$NiSe_2$ Heterostructure

Iron-modified $Ni(OH)_2@NiSe_2$ heterostructure (denoted as Fe-$Ni(OH)_2@NiSe_2$) was synthesized via water bath method. The following steps were involved in the synthesis. Firstly, the mixture solution consisting of 160 mM $NiSO_4 \cdot 6H_2O$, 160 mM $Fe(NO_3)_3 \cdot 9H_2O$ and 90 mM urea was prepared. Among then, $Fe(NO_3)_3 \cdot 9H_2O$ play a vital role in introducing iron into the $Ni(OH)_2@NiSe_2$ heterostructure. Subsequently, the $NiSe_2$ was soaked in the above solution. Then, it was subjected to heating at 70 °C for a duration of 30 min. After the reaction, the obtained Fe-$Ni(OH)_2@NiSe_2$ heterostructures were washed with ultrapure water to removed residual reactants. Finally, the heterostructures were dried under vacuum at 60 °C.

1.2.3 Synthesis of $Ni(OH)_2@NiSe_2$ Heterostructure

The pristine $Ni(OH)_2@NiSe_2$ was manufactured as a control sample by the same preparation procedure except that $Fe(NO_3)_3$ $9H_2O$ was not added.

1.3. Characterization

The morphology of the fabricated self-supporting electrodes was visualized using a Zeiss Sigma 300 field emission scanning electron microscope (FESEM). For higher-resolution images of the electrocatalysts, transmission electron microscopy (TEM) images were acquired using an FEI Tecnai G2-F20 s-twin microscope, operating at an accelerating voltage of 200 kV. X-ray diffraction (XRD) patterns were collected using an X'Pert3 Powder diffractometer with Cu Kα radiation, operating at 40 kV and 40 mA. For chemical analysis, X-ray photoelectron spectroscopy (XPS) spectra were recorded using a K-Alpha+ instrument from Thermo Fisher Scientific, which employed a micro-focused, monochromatic Al-Kα X-ray source with a spot size ranging from 30 to 500 μm. Electron paramagnetic resonance (EPR) spectroscopy were gathered using a JEOL JES-FA200 instrument.

1.4. Electrochemical Measurements

All electrochemical measurements, excluding electrochemical impedance spectroscopy (EIS), were conducted within a three-electrode system employing an electrochemical workstation (Versastat 3). The setup involved the utilization of the as-synthesized self-supporting electrode as the working electrode, a Pt plate as the counter electrode, and an Hg/HgO electrode as the reference electrode. The Nernst equation was applied to convert potential *vs.* Hg/HgO electrode to potential *vs.* reversible hydrogen electrode (RHE):

$$E_{\mathrm{RHE}} = E_{\mathrm{Hg/HgO}} + 0.0059 \times \mathrm{pH} + 0.098$$ [1]

where E_{RHE} represents the potential *vs.* RHE, and $E_{\mathrm{Hg/HgO}}$ signifies the potential *vs.* Hg/HgO electrode. The electrolyte used for the experiments consisted of 1.0 M KOH with or without a 0.33 M urea solution. Linear sweep voltammetry (LSV) curves were recorded over a range from 0 to 0.8 V (*vs.* Hg/HgO) at a scan rate of 5 mV s^{-1}. Operando EIS was conducted within a frequency range spanning from 10^{-2} to 10^{5} Hz, utilizing an AC amplitude of 10 mV by ModuLab XM electrochemical system from Solartron Analytical.

For temperature-dependent measurements, a thermostatic water bath was employed to maintain controlled temperatures. The apparent electrochemical activation energy (E_a) for UOR was determined by Arrhenius relationship:[2]

$$\frac{\partial(\log i_k)}{\partial(1/T)} \Big| = \frac{E_a}{2.3R}$$

where i_k represents the kinetic current at a potential of 1.70 V (*vs.* RHE) under varying temperatures, T signifies the reaction temperature (K), and R stands for the universal gas constant. Arrhenius plots were constructed, and the E_a value was extracted from the slope of these plots.

Figures

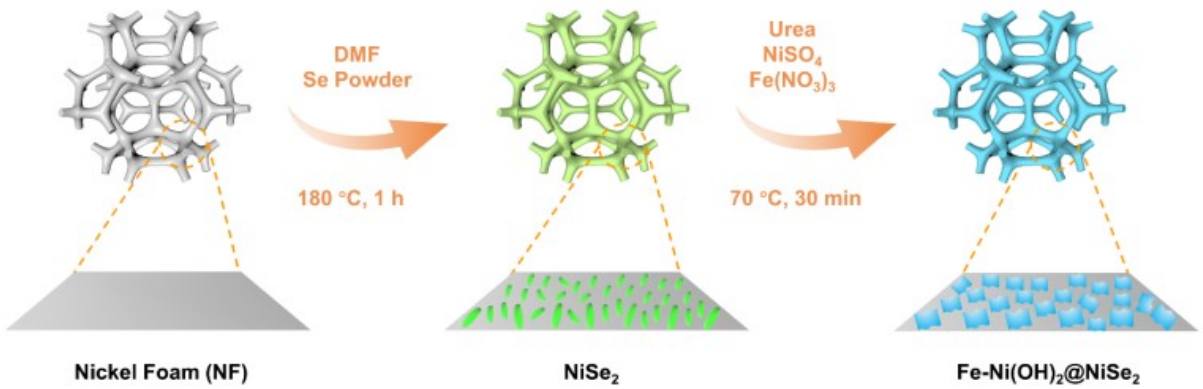

Scheme S1. Preparation process of Fe-Ni$(OH)_2$@$NiSe_2$ electrocatalyst.

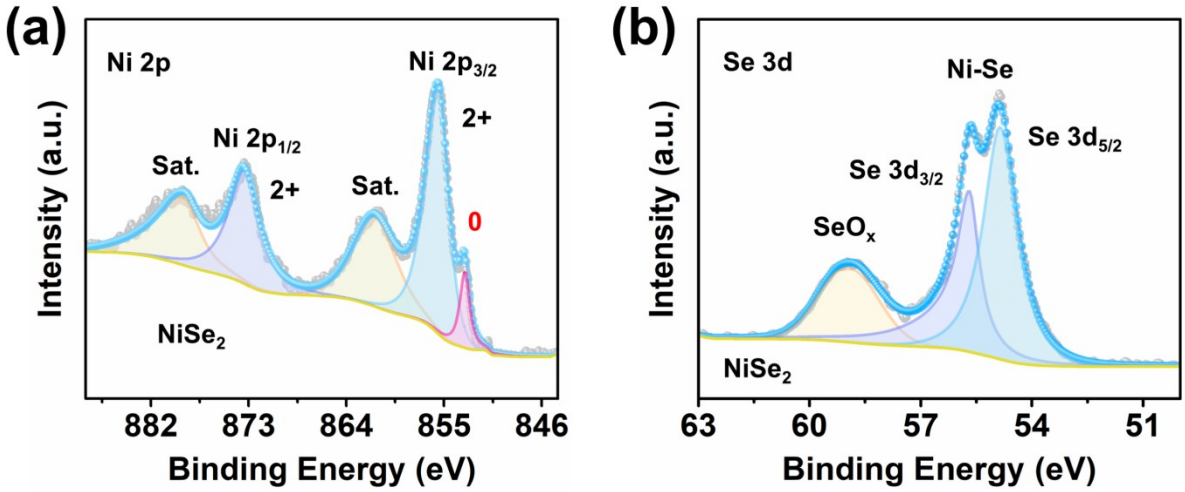

Fig. S1. XPS spectra of $NiSe_2$. (a) Ni 2p and (b) Se 3d.

In the case of $NiSe_2$, the Ni 2p spectra (**Fig.S1a**) displayed binding energy (BE) at 853.04 eV (Ni^0) and 855.49 eV (Ni^{2+}) as well as 870.14 eV (Ni^0) and 873.42 eV (Ni^{2+}) attributed to Ni $2p_{3/2}$ and Ni $2p_{1/2}$,[3] respectively. Concerning the Se 3d spectra (**Fig.S1b**), the BE at 54.85 and 55.70 eV assigned to Se $3d_{5/2}$ and Se $3d_{3/2}$, respectively, suggesting the existence of Ni-Se bonds and Se.[2-4] Furthermore, a BE around 58.9 eV indicates the presence of selenium oxide species.[5]

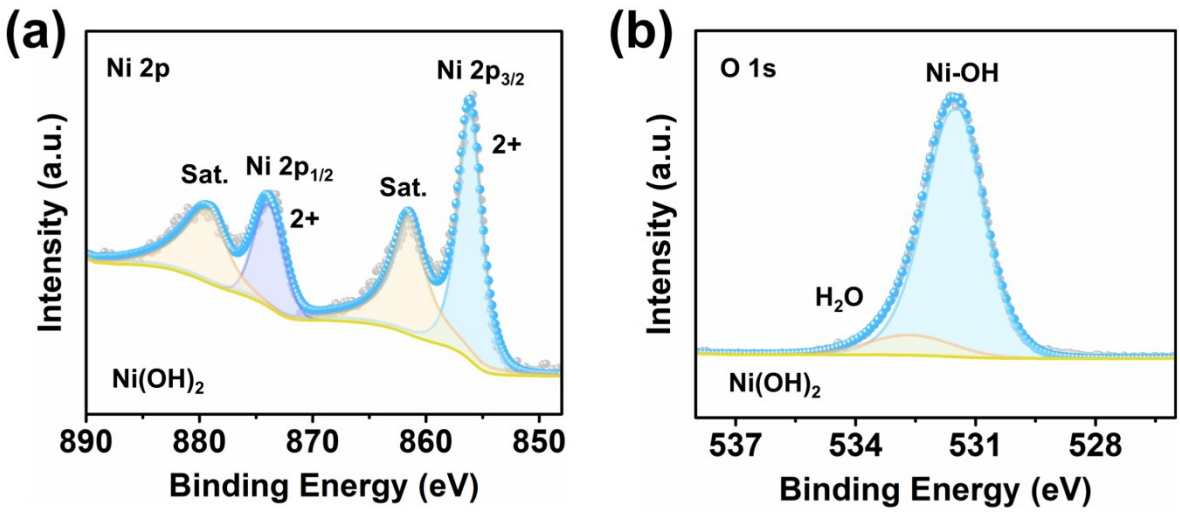

Fig. S2. XPS spectra of $Ni(OH)_2$. (a) Ni 2p and (b) O 1s.

In the case of $Ni(OH)_2$, the Ni 2p spectra (**Fig.S2a**) exhibited BE at 856.11 eV (Ni $2p_{3/2}$) and 873.87 eV (Ni $2p_{1/2}$), characteristic of Ni^{2+}.[6] For the O1s spectra (**Fig.S2b**), the BE at 531.44 and 532.63 eV linked to Ni-OH and absorbed H_2O from air,[7] respectively.

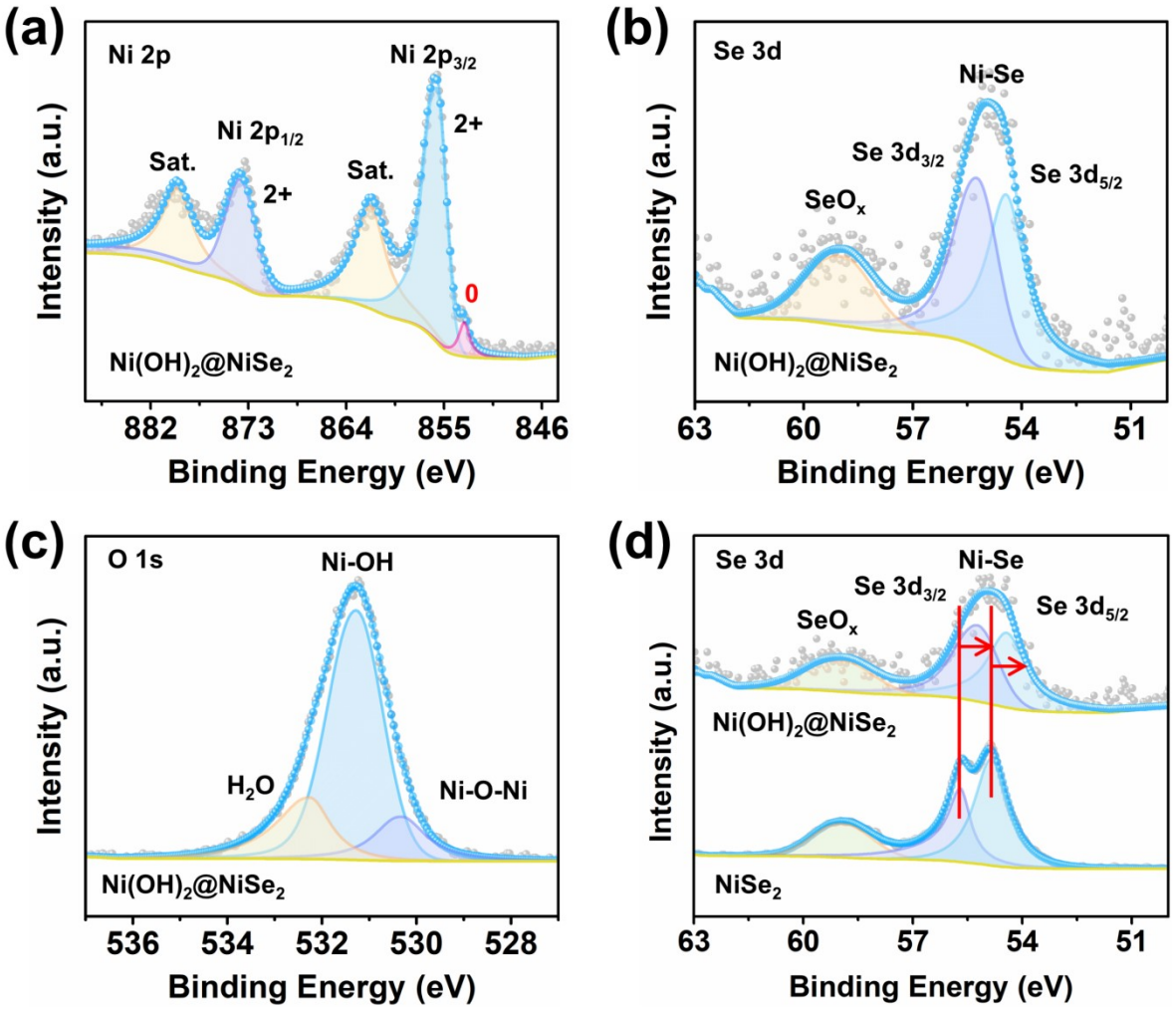

Fig. S3. XPS spectra of $Ni(OH)_2$@$NiSe_2$ heterojunction. (a) Ni 2p, (b) Se 3d, and (c) O 1s. (d) XPS spectra of Se 3d in $NiSe_2$ and $Ni(OH)_2$@$NiSe_2$.

Notably, the $Ni(OH)_2$@$NiSe_2$ heterojunction revealed a more complex Ni $2p_{3/2}$ spectrum, as shown in **Fig.S3a**, with three peaks at 853.16, 855.69 and 861.77 eV were attributed to the Ni^0, Ni^{2+} and satellite peaks,[8] respectively. Correspondingly, the Ni $2p_{1/2}$ spectrum exhibited fitted peaks at 873.74 and 879.55 eV, associated with Ni^{2+} and satellite peaks,[9] respectively. The Se 3d spectra (**Fig.S3b**) displayed BE of 54.42 and 55.22 eV corresponding to Se $3d_{5/2}$ and Se $3d_{3/2}$, elucidating the presence of Ni-Se bonds. For the O 1s spectra (**Fig.S3c**), the BE at 530.99, 531.58 and 532.86 eV were consistent with Ni-O-Ni, Ni-OH/oxygen vacancy and absorbed H_2O from air, respectively. It is noteworthy that the Se 3d spectrum of

$Ni(OH)_2$@$NiSe_2$ was shifted towards the lower binding energy relative to the that of $NiSe_2$ (**Fig.S3d**) compared to pure $NiSe_2$, signifying that the electrons transfer from $Ni(OH)_2$ to the surface $NiSe_2$, culminating in the establishment of a stable heterogeneous interface with a strong electron interaction between $Ni(OH)_2$ and $NiSe_2$.

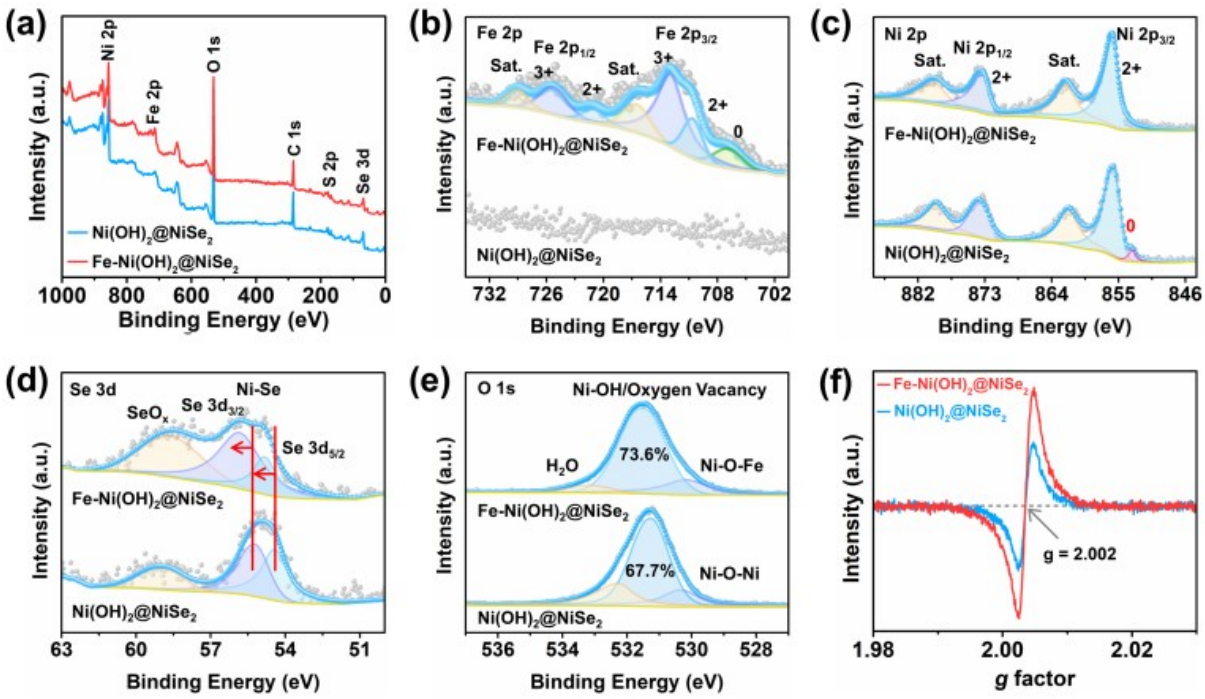

Fig. S4. (a) XPS survey. XPS spectra of (b) Fe 2p, (c) Ni 2p, (d) Se 3d, and (e) O 1s in both $Ni(OH)_2@NiSe_2$ and $Fe\text{-}Ni(OH)_2@NiSe_2$. (f) EPR.

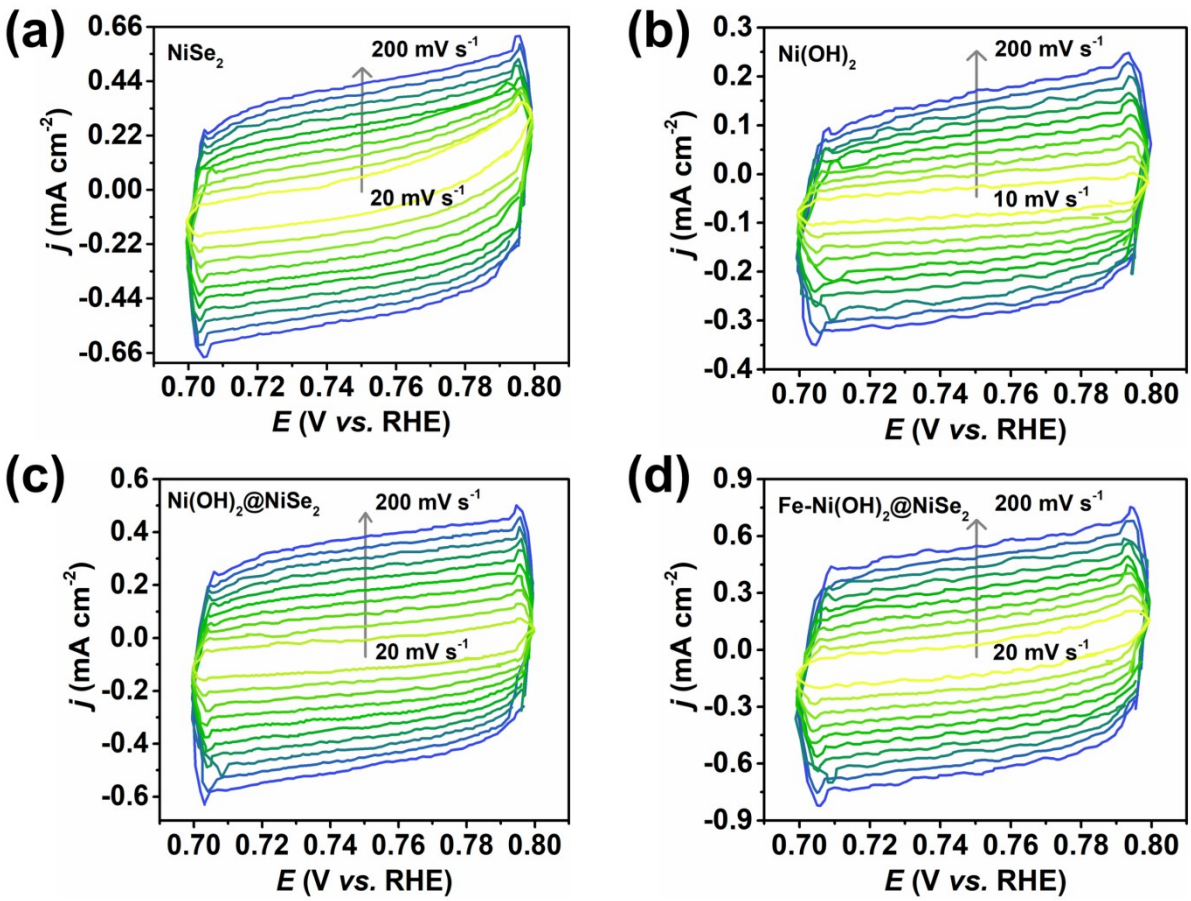

Fig. S5. Electrochemical double-layer capacitance (C_{dl}) of (a) $NiSe_2$, (b) $Ni(OH)_2$, (c) $Ni(OH)_2$@$NiSe_2$, and (d) Fe-$Ni(OH)_2$@$NiSe_2$.

ECSA was determined by measuring the capacitive current associated with double-layer charging from the scan-rate dependence of CVs. For this, the potential window of CVs was 0.7 ~ 0.8 V *vs.* RHE. The scan rates were 20, 40, 60, 80, 100, 120, 140, 160, 180 and 200 mV s^{-1}. The double-layer capacitance (C_{dl}) was estimated by plotting the $\Delta J = J_a - J_c$ against the scan rate. The linear slope is twice of the double layer capacity. The ECSA values were calculated from the measured double layer capacitance divided by the specific capacitance (C_s; ~40 μF cm^{-2}) via ECSA = C_{dl}/C_s [10].

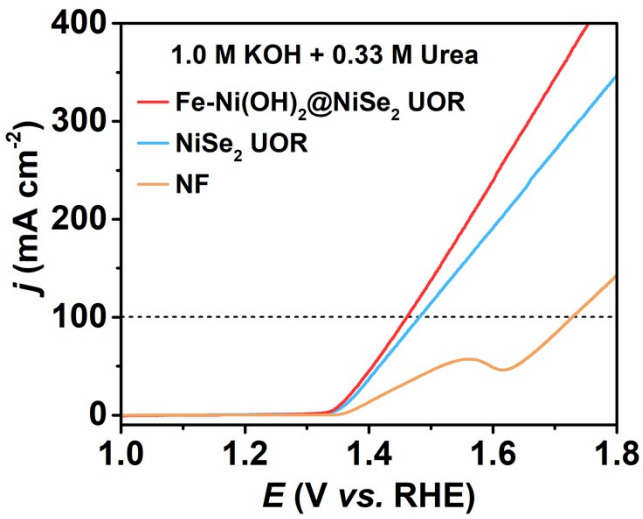

Fig. S6. LSV curves of NF, $NiSe_2$, and Fe-$Ni(OH)_2$@$NiSe_2$.

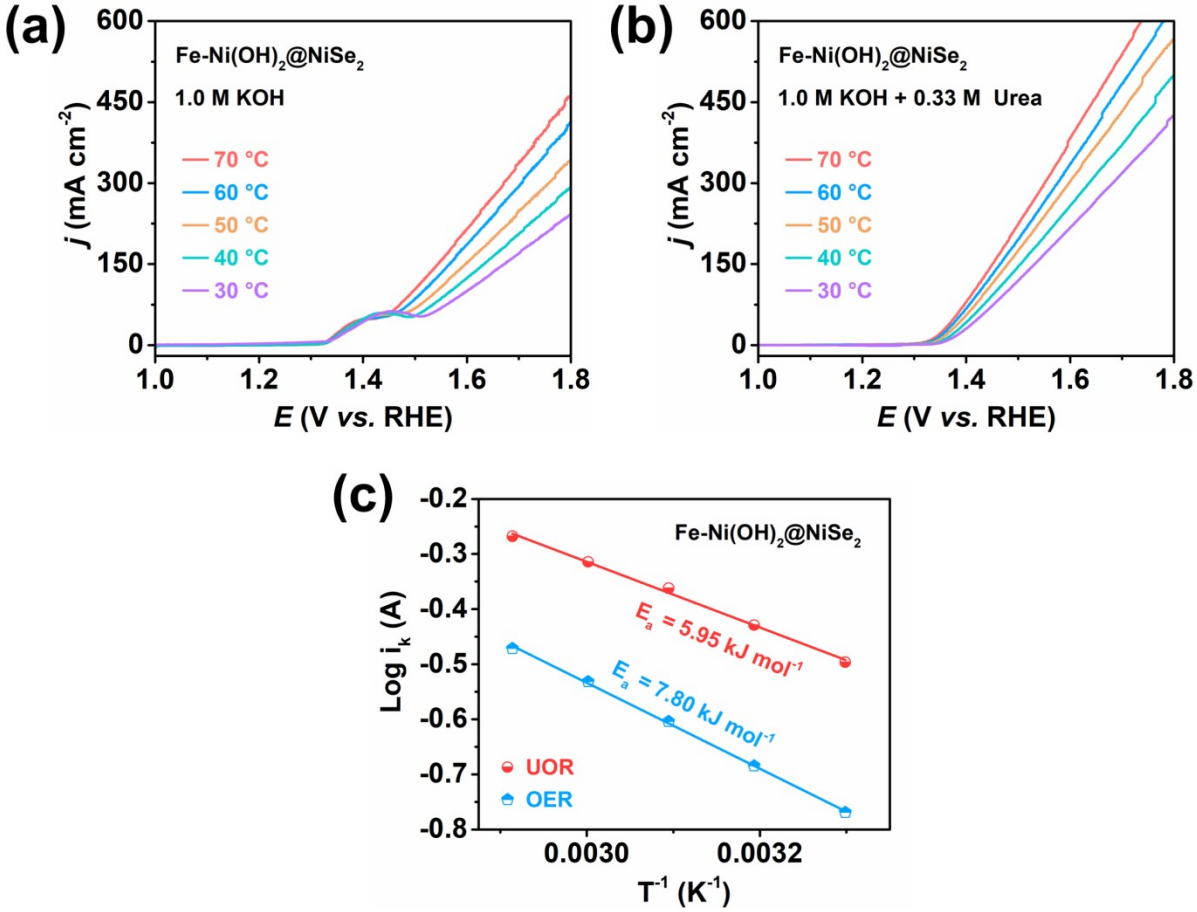

Fig. S7. Temperature-dependent electrocatalytic performances of Fe-Ni$(OH)_2$@$NiSe_2$ in (a) 1.0 M KOH, and (b) in 1 M KOH with 0.33 M urea at 30 °C, 40 °C, 50 °C, 60 °C, and 70 °C, respectively. (c) Arrhenius plot of Fe-Ni$(OH)_2$@$NiSe_2$ in 1.0 M KOH (*i.e.,* UOR) and without (i.e., OER) 0.33 M urea, at 1.70 V *vs.* RHE.

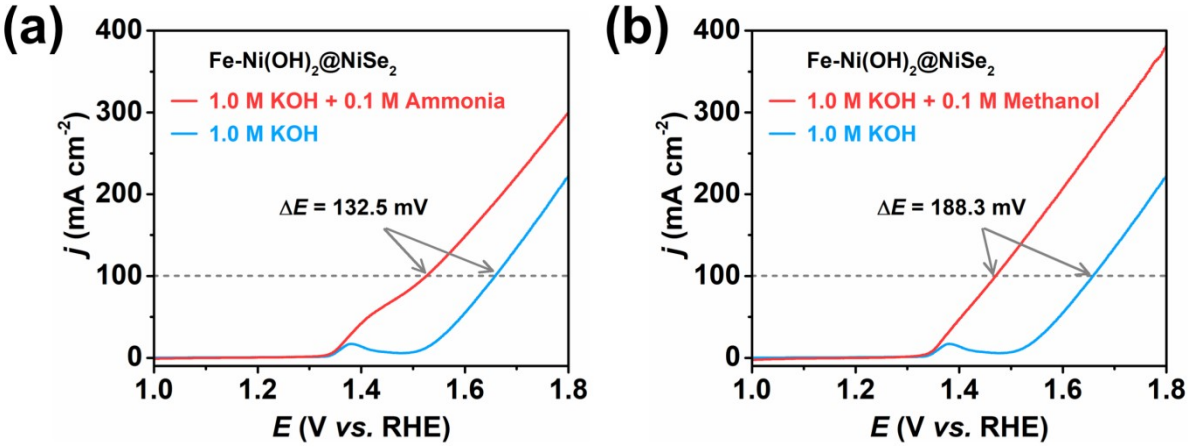

Fig. S8. The LSV curves of Fe-Ni$(OH)_2$@$NiSe_2$ in 1.0 M KOH with and without the addition of (a) 0.1 M ammonia and (b) methanol.

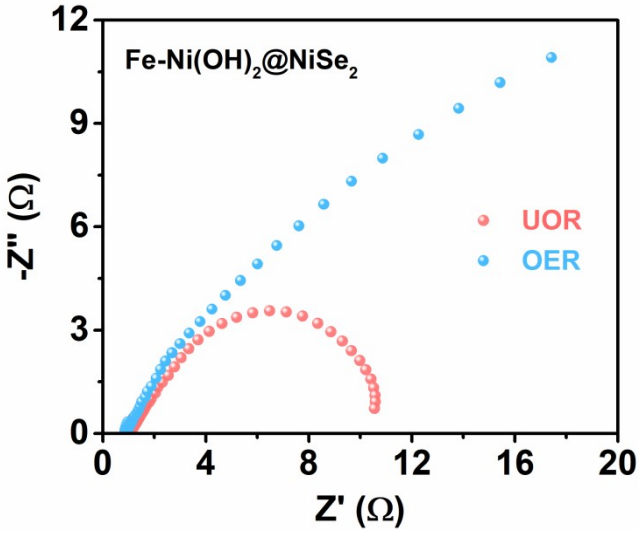

Fig. S9. Nyquist plots of the OER (1 M KOH) and UOR (1 M KOH with 0.33 M urea) for Fe-$Ni(OH)_2$@$NiSe_2$.

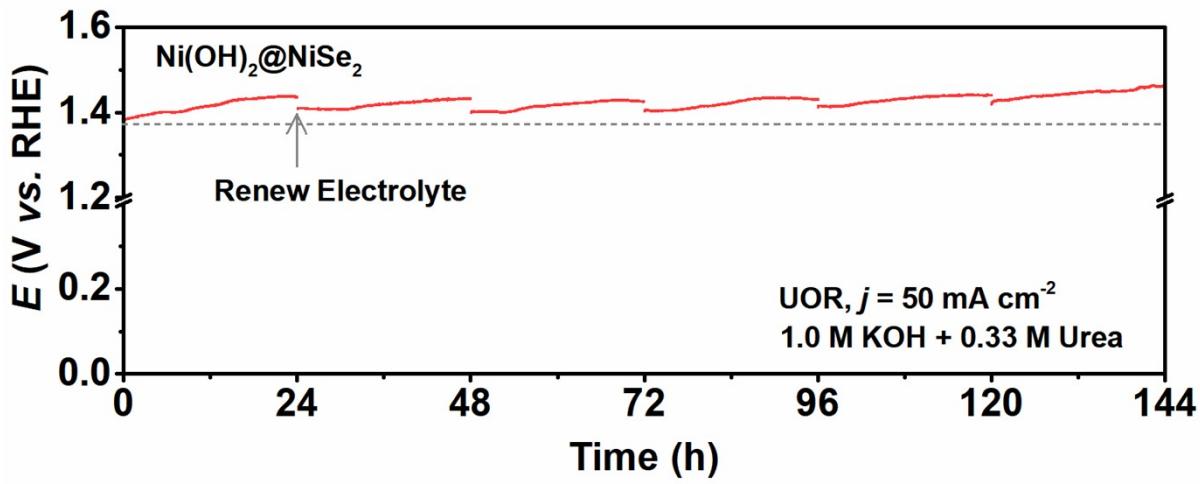

Fig. S10. Chronopotentiometry test of $Ni(OH)_2$@$NiSe_2$ in 1.0 M KOH with 0.33 M urea.

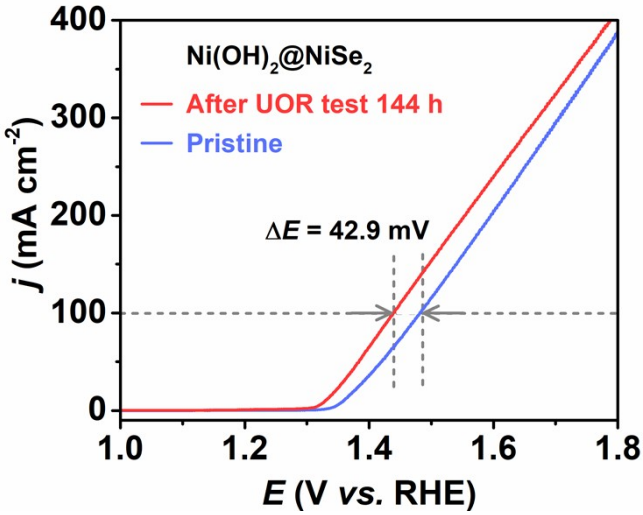

Fig.S11. LSV curves of $Ni(OH)_2$@$NiSe_2$ in 1.0 M KOH with 0.33 M urea.

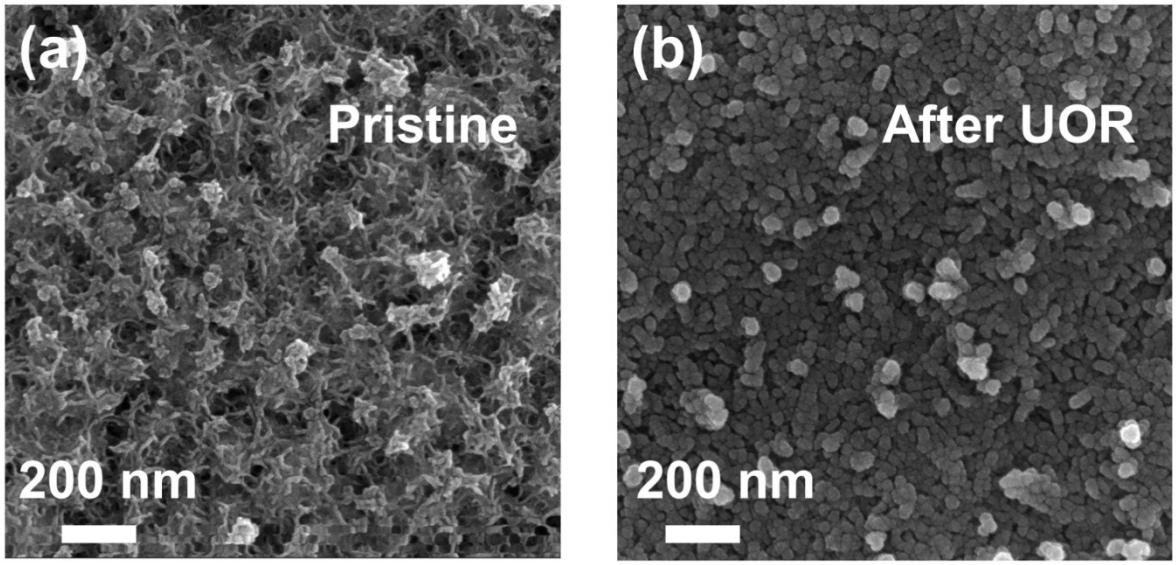

Fig. S12. SEM images of Fe-Ni$(OH)_2$@$NiSe_2$ both (a) pristine and (b) after UOR.

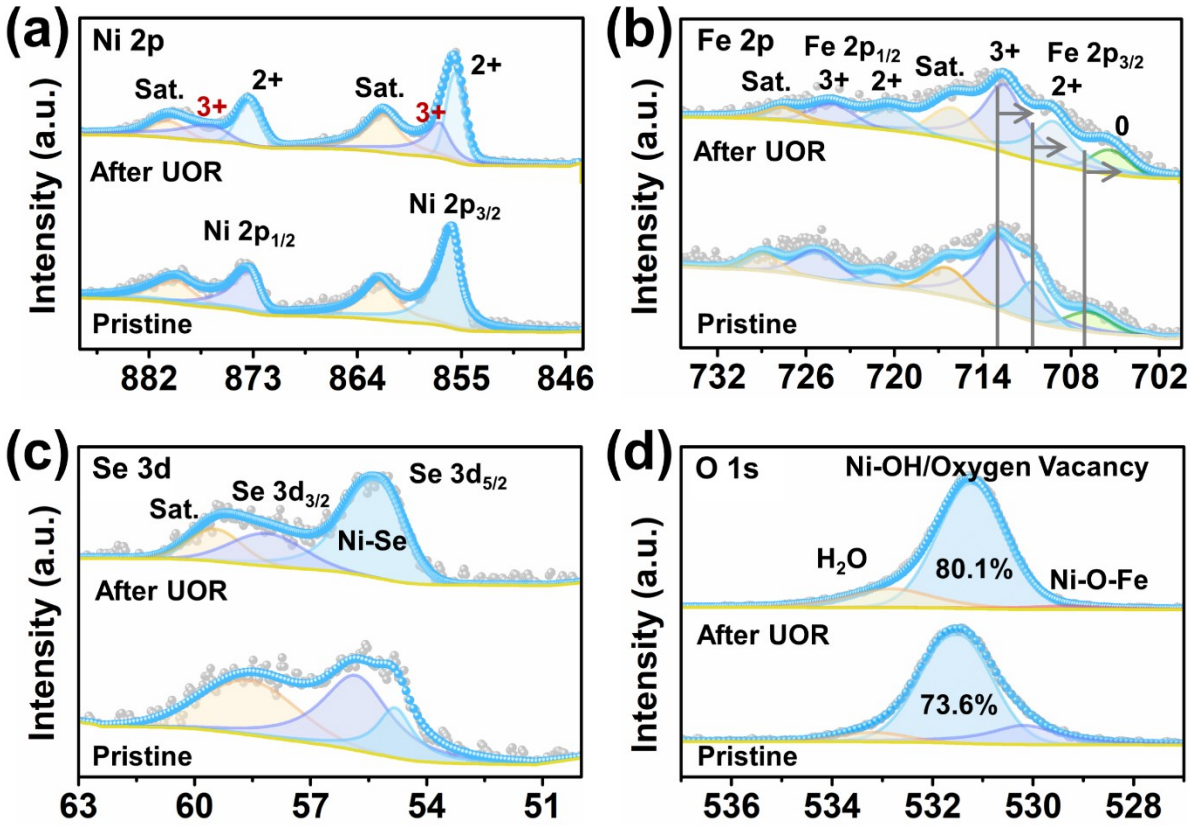

Fig. S13. XPS spectrum of Fe-Ni$(OH)_2$@$NiSe_2$ both pristine and after UOR. (a) Ni 2p, (b) Fe 2p, (c) Se 3d, and (d) O 1s, respectively.

Fig. S13 reveals the changes of catalyst in chemical composition before and after participates in the UOR process. After the UOR process, a characteristic peak corresponding to Ni^{3+} was observed in the Ni 2p orbitals, indicating the oxidation of Ni to a high-valent nickel species (Ni^{3+}). In the Fe 2p orbitals, the presence of zero-valent Fe suggests that Fe acts as an electron acceptor, facilitating the oxidation of Ni to a high-valent Ni species. In the Se 3d orbitals, a leftward shift in the binding energy positions of Se $3d_{3/2}$ and Se $3d_{5/2}$ indicates the oxidation of Se during the electrochemical process. In the O 1s orbitals, the increase in the content of O-H bonds observed indicates the generation of more NiOOH species during the electrochemical process.

References

1. L. Zhai, T. W. Benedict Lo, Z. Xu, J. Potter, J. Mo, X. Guo, C. C. Tang, S. C. Edman Tsang and S. P. Lau, *ACS Energy Lett*, 2020, **5**, 2483-2491.
2. Q. Wen, Y. Lin, Y. Yang, R. Gao, N. Ouyang, D. Ding, Y. Liu and T. Zhai, *ACS Nano*, 2022, **16**, 9572-9582.
3. Z. Ye, P. Li, W. Wei, C. Huang, L. Mi, J. Zhang and J. Zhang, *Adv Sci*, 2022, **9**, e2200067.
4. S. F. Zai, X. Y. Gao, C. C. Yang and Q. Jiang, *Adv Energy Mater*, 2021, **11**, 2101266.
5. K. Huang, C. Lin, G. Yu, P. Du, X. Xie, X. He, Z. Zheng, N. Sun, H. Tang, X. Li, M. Lei and H. Wu, *Adv Funct Mater*, 2022, **33**, 2211102.
6. W. Wang, Y. Wang, R. Yang, Q. Wen, Y. Liu, Z. Jiang, H. Li and T. Zhai, *Angew Chem Int Edit*, 2020, **59**, 16974-16981.
7. B. Zhou, Y. Li, Y. Zou, W. Chen, W. Zhou, M. Song, Y. Wu, Y. Lu, J. Liu, Y. Wang and S. Wang, *Angew Chem Int Edit*, 2021, **60**, 22908-22914.
8. N. Chen, Y. X. Du, G. Zhang, W. T. Lu and F. F. Cao, *Nano Energy*, 2021, **81**, 105605.
9. Q. Sun, L. Wang, Y. Shen, M. Zhou, Y. Ma, Z. Wang and C. Zhao, *ACS Sustainable Chem Eng*, 2018, **6**, 12746-12754.
10. P. Liu, B. Chen, C. W. Liang, W. T. Yao, Y. Z. Cui, S. Y. Hu, P. C. Zou, H. Zhang, H. J. Fan and C. Yang, *Adv Mater*, 2021, **33**, 2007377.